This is the Pre-Published Version.

The following publication Zhou, G., Lu, F., Shang, S., Shou, D., Wang, W., Yu, K., ... & Hu, E. (2023). Gas-jet propelled hemostats for targeted hemostasis in wounds with irregular shape and incompressibility. Journal of Materials Chemistry B, 11(17), 3885-3897 is available at https://doi.org/10.1039/D3TB00165B.

Gas-jet propelling hemostats for targeted hemostasis in wounds with irregular shape and incompressibility

Guofang Zhou [1], Fei Lu [1], Songmin Shang [2], Dahua Shou [2], Wenyi Wang [3]*, Kun Yu [1], Ruiqi Xie [1,2], Guangqian Lan [1,4], Enling Hu [1,2,4]*

[1] *State Key Laboratory of Silkworm Genome Biology, College of Sericulture, Textile and Biomass Sciences, Southwest University, Chongqing 400715, China*

[2] *School of Fashion and Textiles, The Hong Kong Polytechnic University, Hong Kong*

[3] *Department of Applied Biology and Chemical Technology, The Hong Kong Polytechnic University, Hong Kong*

[4] *Chongqing Engineering Research Center of Biomaterial Fiber and Modern Textile, Chongqing 400715, China*

***Corresponding author:**

Email: enling.allen.hu@connect.polyu.hk (Enling Hu)

Address:

Dr Enling Hu

School of Fashion and Textiles

Room QT715, Q Core, 7/F

The Hong Kong Polytechnic University

Hung Hom, Kowloon, Hong Kong

Abstract:

Since the hemostats are likely flushed off from the wound by massive gushing blood, achieving rapid and effective hemostasis in complex bleeding wounds with powder hemostats continues to be a significant therapeutic challenge. In order to counter the flushing effect of gushing blood, a gas-jet propelled powder hemostat ($(COL/PS)_4@CaCO_3$-T-TXA^+) is developed. $(COL/PS)_4@CaCO_3$-T-TXA^+ dives into the deep bleeding sites of complex wounds for the targeted hemostasis. In preparation, protamine sulfate and collagen are first electrostatically deposited on $CaCO_3$, which is then loaded with thrombin, and finally doped with protonated tranexamic acid (TXA-NH_3^+) to produce the final therapeutic medicine $(COL/PS)_4@CaCO_3$-T-TXA^+. When applied to bleeding tissues, $CaCO_3$ and TXA-NH_3^+ from $(COL/PS)_4@CaCO_3$-T-TXA^+ immediately reacts to each other in blood to release countless CO_2 macro bubbles, which directs the hemostatic powder, $(COL/PS)_4@CaCO_3$-T-TXA^+, precisely towards deep bleeding sites from the complex wounds. Then the carried thrombin is released to accomplish the targeted hemostasis. $(COL/PS)_4@CaCO_3$-T-TXA^+ has better effects in rabbit hepatic hemorrhage models, according to animal studies; the hemorrhage quickly stops within 30 s, which is roughly 20% less than the commercial product Celox^{TM}. The present study provides a new strategy for using powder hemostats to quickly and effectively stop bleeding in complex bleeding wounds.

Keywords: targeted hemostasis, powder hemostat, gas-jet propelling, drug delivery, complex bleeding wounds

1 Introduction

Whether in a military conflict or a civilian incident, excessive bleeding poses a life-threatening risk [1, 2]. When the blood loss exceeds more than 20% of the body's total blood volume, complications like shock may occur [3]. Additionally, handling, shipping, and storage requirements for blood would result in significant medical costs from blood transfusions [4]. Therefore, efficient hemostatic products are crucial. An effective hemostatic material should quickly absorb blood and aggregate together blood cells and platelets to effectively control excessive bleeding.

Different types of hemostatic materials have been developed as of late. To achieve hemostasis, for instance, conventional gauze [5] and sponge [6] absorb blood liquid and concentrate coagulation components [7, 8]. However, because of their low adaptability to complicated wound profiles, which results in deficient hemostasis performance, they are inappropriate for complex wounds, such as incompressible wounds and those with irregular shapes. To tackle this, adhesive hydrogels were developed to seal the bleeding wound for hemostasis. However, there was still a significant chance that the hydrogel would slip off from bleeding wounds that prevented hemostasis from occurring because blood infiltration into the hydrogel would weaken its adhesiveness [9]. Given the nature of irregular wounds, powder hemostats could assist hemostasis more effectively than conventional hemostats, as they could adaptively deposit to bleeding wound beds [10, 11].

Although various commercial powder hemostatic materials have been developed in

recent decades, such as QuikClot^{TM} and Celox^{TM}, they still have drawbacks that cannot be overlooked. For instance, QuikClot zeolite power was designed for high-pressure bleeding. However, due to its exothermic reactivity and limited biodegradability, it could induce severe tissue damage and foreign body reactions [12, 13]. More importantly, the biggest concern with powder materials is that their hemostatic efficacy may suddenly deteriorate when there is heavy bleeding. They couldn't deposit to the hidden or deep bleeding sites in the interior of the wound, and the blood gushing from the wound was likely going to flush them away.

Therefore, there is a high demand for developing intelligent powder hemostatic materials. At least two systems, a drug carrier system for mounting hemostatic drugs and a driving-force-generation system for delivery of drug carrier, must be present in the featured structure of powder hemostatic composites. In contrast to traditional powder hemostats, this one will intelligently self-dive in blood, deposit at the wound's base exactly where the bleeding sites were, and then release drugs to activate hemostasis at the affected bleeding sites. To ensure the effectiveness of powder hemostatic materials in severe hemorrhage, the structural design of the intelligent self-driving platform for hemostat delivery was crucial.

Potential drug nanocarriers with considerable drug loading include calcium electrolytes, such as calcium phosphide, tricalcium phosphate, and calcium carbonate ($CaCO_3$) [14]. As a non-toxic natural biological mineral, $CaCO_3$ is particularly well suited due to its

outstanding biocompatibility, biodegradability, and pH sensitivity [15]; crystal $CaCO_3$ has already demonstrated incredible potential for building clever vectors for medicines, DNA, and proteins. In light of this, layer-by-layer (LBL) assembly allowed for the functionalization of it with polyelectrolytes to create organic-inorganic hybrid drug carriers, which not only increased the number of pharmaceuticals that can be loaded but also gave it more functionality [16]. Examples include the usage of $CaCO_3$ coupling with dextran/poly-L-arginine for the drug delivery system for bull serum albumin [17], poly-L-ornithine/fucoidan-coated $CaCO_3$ particles with pH-controlled release for cancer therapy [18], and chitosan/sodium alginate-coated mesoporous $CaCO_3$ to transport folic acid for precise molecular targeting and drug release [16]. This evidence revealed that $CaCO_3$ had a bright future and was useful, particularly when combined with coating materials.

Protamine sulfate (PS), a biodegradable cationic peptide produced from fish sperm, is positively charged as a result of its high arginine content. PS is also a possible biocompatible natural agent for drug delivery because of the powerful electrostatic contact caused by its negatively charged groups. Natural PS and sodium alginate have been utilized to change a drug delivery system via electrostatic attraction in order to increase the effectiveness of anti-cancer drug delivery [19]; a similar study also employed PS to modify graphene hybrid film for antibacterial [20]. Given that PS has been used in hemostasis as well [21], it would be useful to use PS when developing smart powder hemostatic materials.

Currently, a variety of polymers, such as chitosan [22], calcium alginate [23], fibrin [24], gelatin [25], collagen [26], oxidized cellulose [27], and oxidized regenerated cellulose[28], have been widely used in biomaterials due to their superior high water absorption, fibrinogen adsorption, macrophage phagocytosis activation, platelet aggregation promotion, and antibacterial activity. Given its strong bioactivity in hemostasis, low antigenicity, outstanding biocompatibility, and high cell proliferation, collagen—a naturally occurring, biodegradable, negatively charged macromolecule—has been widely used as a hemostatic dressing [29], wound dressing [30], and tissue engineering scaffold [31, 32]. Additionally, collagen has the ability to stimulate platelet adhesion and aggregation as well as the release of coagulation factors to aid in blood coagulation [33, 34]. Collagen was a useful addition to the structure of the intelligent powder hemostatic materials since it has been hypothesized that it can work in concert with thrombin to improve hemostatic performance [35].

Therefore, in this investigation, we first designed a hemostatic agent, called $(COL/PS)_4@CaCO_3$-T-TXA^+, in order to address the challenges highlighted in hemorrhage control in irregular shaped and uncompressible wounds with powder hemostatic materials. The preparation process involved three steps (Fig. 1): (1) coating $CaCO_3$ with PS (positively charged) and Type I collagen (negatively charged) using LBL self-assembly to create $(COL/PS)_4@CaCO_3$, which served as the essential drug carrier; (2) loading thrombin into the $(COL/PS)_4@CaCO_3$ drug carrier to produce

(COL/PS)$_4$@$CaCO_3$-T, which was the drug delivery platform mounted with drugs; and (3) finally, (COL/PS)$_4$@$CaCO_3$-T was doped with protonated tranexamic acid (TXA-NH_3^+), resulting in (COL/PS)$_4$@$CaCO_3$-T-TXA^+, which was endowed with gas-jet propelling capability and was capable of accurately diving into the deep bleeding areas of wounds for targeted hemostasis.

The primary goal of the current study was to use intelligent powder hemostats to address the fundamental problem of hemostasis for severe bleeding. It provides a different viewpoint for precise hemostasis at deep, hidden bleeding sites in wounds with irregular shape and incompressibility. In addition to being appropriate for the conveyance of hemostatic medications, the gas-jet delivery platform was also available for other therapies that demanded for in vivo drug delivery.

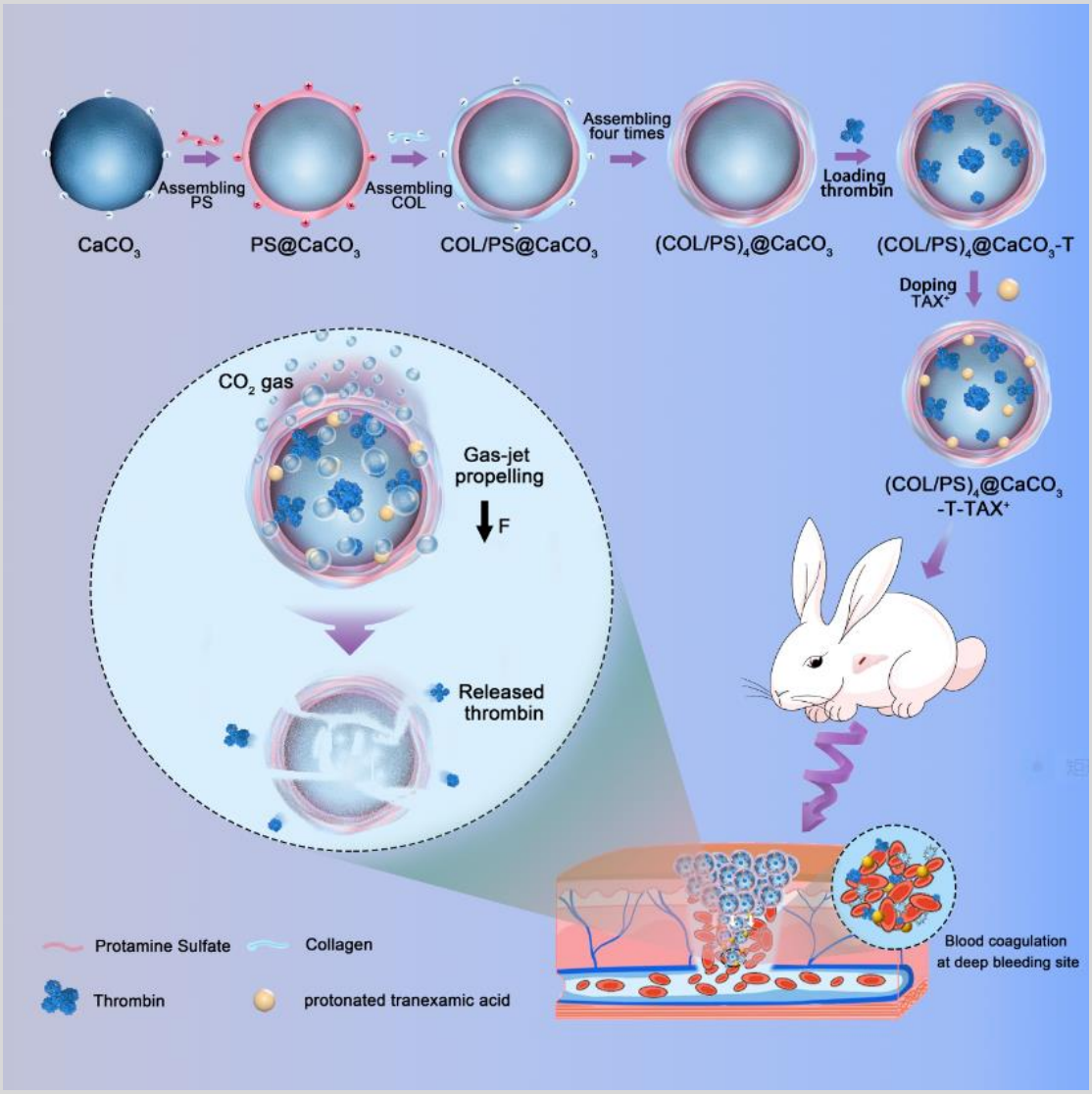

Fig. 1 Preparation of $(COL/PS)_4@CaCO_3$-T-TXA-NH_3^+ and its hemostatic mechanism

2 Experimental

2.1 Chemicals and reagents

All of the chemicals, reagents, and organic solvents were of the highest purity analytical grade and were purchased and used without further purification. Bovine thrombin (T) (100 U mg^{-1}) was purchased from Sigma-Aldrich Co., Ltd. (St. Louis, MO, USA). The PS was purchased from Yuanye Bio-Technology Co., Ltd (Shanghai, P. R. China). Cell Counting Kit-8 (CCK-8), fluorescein isothiocyanate (FITC)-annexin V/Propidium

iodide (PI) Cell Apoptosis Kit were purchased from Thermo Fisher Scientific Co., Ltd. (Shanghai, P. R. China). Fluorescent thrombin substrate (Boc-Val-Pro-Arg-MCA) was purchased from Peptide Institute, Inc. (Minoh-shi, Osaka, Japan). The National Teaching Center of Animal Science and Experiment of Southwest University in China authorized the procedures for all the animal studies, and they were carried out in accordance with those approved by the committee on animal ethics (accreditation number of the investigator: CQLA-2019-0281).

2.2 Material preparation

$CaCO_3$: $CaCl_2$ (200 mM, 50 mL) and Na_2CO_3 (200 mM, 50 mL) were combined while being stirred for 60 s. The precipitate was then centrifuged (3000 rpm for 2 min), repeatedly rinsed with deionized water three times, and dried for 24 h at 50 ºC. $CaCO_3$ was successfully prepared for usage later.

COL: Tilapia skins (20 g) were divided into small pieces (about 5×5 mm), and then sequentially exposed to NaOH (0.1 M, 400 mL) for 24 h and HAc (0.5 M, 1.1 L) for 2 d. The mixture was dialyzed for 1 d after the supernate was removed to extract the collagen, which was then further freeze-dried before usage.

$(COL/PS)_4@CaCO_3$-T: Deionized water was first used to prepare a $CaCO_3$ dispersion (0.33 M), while NaCl solution (0.2 M) was used to prepare PS (0.5 mg/mL) and COL (1.0 mg/mL) solutions. To create opposing charges that can adsorb one another LBL,

the pH values of PS and COL solutions were adjusted to 7.9 with the use of 0.1 M HCl or NaOH solutions. Then, while vibrating at 37 ^{o}C for 20 min, PS (0.5 mg/mL, 5 ml) and COL (1 mg/mL, 5 ml) were successively adsorbed on the $CaCO_3$ (0.33 M, 5 ml) in each LBL assembly cycle. The samples were centrifuged at 2,000 rpm for 2 min following each cycle, and then they were washed twice with NaCl solution (0.2 M). To prepare $(COL/PS)_4@CaCO_3$, the LBL assembly cycle was repeated four times, followed by the sample being dried in a vacuum-assisted freeze drier (for comparison, the LBL assembly was also conducted in one, two, and three cycles to prepare $COL/PS@CaCO_3$, $(COL/PS)_2@CaCO_3$ and $(COL/PS)_3@CaCO_3$). Finally, $(COL/PS)_4@CaCO_3$ particle suspension (10%, w/v) was loaded with bovine thrombin (200 U/mL, 0.1 mL) to obtain $(COL/PS)_4@CaCO_3$-T.

$(COL/PS)_4@CaCO_3$-T-TXA^+: First, 0.1 M HCl solution was added to 0.5 M TXA-NH_2 until the pH reached 4.3. After lyophilization, the solid TXA-NH_3^+ was collected. The next step was to produce $(COL/PS)_4@CaCO_3$-T-TXA_3^+ by mixing $(COL/PS)_4@CaCO_3$-T particles with TXA-NH_3^+ at an identical molar ratio. For comparison, $(COL/PS)_4@CaCO_3$ without thrombin was also doped with TXA-NH_3^+ to prepare $(COL/PS)_4@CaCO_3$-TXA^+ for particular tests.

2.3 Material characterization

Scanning electron microscope (SEM), X-ray diffraction (XRD), Fourier transform infrared spectroscopy (FTIR), and thermal gravimetric analysis (TGA) in the nitrogen

flow were used for characterization. The ζ potential was measured on a Zetasizer Nano instrument (Malvern Instruments, Malvern, UK), and surface wettability was assessed by a contact angle goniometer (JY-PH, Chengde Jinhe Instruments, China).

2.4 Evaluation of gas-jet propelling ability

Glass tubes (4 mm in internal diameter) filled with phosphate-buffered saline (PBS; pH 7.4) were utilized to evaluate the gas-jet propelling property. Fluorescent isothiocyanate labeled $(COL/PS)_4@CaCO_3$-T-TXA^+ (namely FITC-$(COL/PS)_4@CaCO_3$-T-TXA^+) was injected into the glass tubes that fixed at various angles (90°, 45°, 0°, 45°, and 90°) in the horizontal direction. Following complete stabilization of the propelling FITC-$(COL/PS)_4@CaCO_3$-T-TXA^+, the propulsion distance was determined using a ruler under ultraviolet light (wavelength: 365 nm).

2.5 Evaluation of clotting ability and *in vitro* hemostasis

The hemostatic performance was assessed using two different methods: (1) the well plate approach, which was initially used to detect blood clotting [10], where mixed samples in wells were photographed every minute; and (2) the classical method, which assessed the entire blood clotting time [36]. For both techniques, a 100 mg dosage of hemostatic material was used.

A plastic blood-transporting tube with an inner diameter of 4 mm was implanted in a pig liver in order to mimic bleeding from uncompressible wounds (Fig. 2). By using a

microinjection device (BYZ-810 T, Hunan, China), blood was pre-added with citric acid and pushed at a rate of 40.0 mL/s from the input to the output. In order to monitor the hemostatic status and track the hemostatic time, particulate hemostats were placed to the injury point as soon as blood started to leak from it.

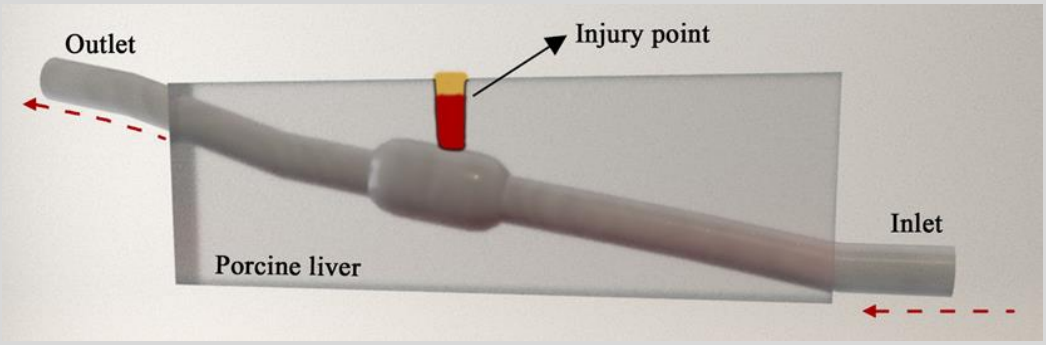

Fig. 2 Schematic diagram of in vitro porcine liver hemostasis model

2.6 Investigation of blood coagulation mechanisms

Red blood cell adhesion: Blood cell solutions were added to samples and cultivated for 1 h at 37 °C. After that, adherent blood cells were fixed with 2.5 weight percent glutaraldehyde overnight and gradually dehydrated using a 10% interval between each of the following ethanol solutions: 50%, 60%, 70%, 80%, 90%, and 100%. Nonadhered blood cells were then removed by washing with PBS three times. The dried samples were examined using SEM after 12 h of drying at 37 °C.

Platelet activation: According to previously published research [37], the effect of platelet activation of $(COL/PS)_4@CaCO_3$ was evaluated. $CaCO_3$ served as the negative control while Ca^{2+} served as the positive control. Additionally, FITC-PAC-1 and AF647-CD61

were used to label the activated platelet and the whole platelet, respectively. Fluorescence-activated cell sorting (FACS), performed with a BD CytoFLEX V5-B5-R3 Flow Cytometer (Franklin Lakes, NJ), was used to determine the activation of platelets in blood.

2.7 Assessment of *in vivo* hemostasis

Mouse aged 7-9 weeks were used in the animal studies (weight of 200–250 g, male). The mouse tail vein and femoral artery served as models for testing the hemostasis. Each mouse was immobilized on a plastic plate after receiving a 10 wt% chloral hydrate injection (0.5 mL per 100 g of the animal). The left leg of the mice was dissected to expose the femoral artery, which was then cut off using a scalpel to create the femoral artery model. Further animal tests were performed on 12 New Zealand White rabbits. On an operating table, each rabbit was immobilized after receiving an intramuscular injection of xylazine hydrochloride (0.2 mL per kilogram of the animal). An 8 mm depth cut was made in the rabbit liver to establish the uncompressible wound model. 0.1 g $(COL/PS)_4@CaCO_3$-T-TXA^+ or Celox^{TM} was then applied to the wound region after the damage. Instantaneously, the hemostasis time was recorded (four replicates for each damage).

2.8 Study on hemocompatibility, cytocompatibility and biodegradability

According to published work [38], the hemolysis activity of $(COL/PS)_4@CaCO_3$ was studied. $(COL/PS)_4@CaCO_3$ was added to anticoagulant-containing erythrocyte stocks

(100 µl). Deionized water served as the positive control and PBS as the negative control in the control groups. Cell Counting Kit-8 (CCK8) assay was used to test the cell viability of $(COL/PS)_4@CaCO_3$ using mouse fibroblast (L929) cells [39]. The subcutaneous implantation model, which has been previously reported [40], was used to evaluate the $(COL/PS)_4@CaCO_3$'s vivo degrading property and host response.

2.9 Statistical analyses

Data were presented as mean ± standard deviation (SD). Statistical analyses were performed using Origin 2017 software. One-way analysis of variance (ANOVA) followed by Tukey's post hoc test or unpaired Student's t-test, two-tailed, was employed to examine the statistical significance where appropriate. Statistical significance was assessed at *p <0.05, **p < 0.01 and ***p < 0.001.

3 Results and discussion

3.1 Characterization

$(COL/PS)_4@CaCO_3$ was created using an LBL technique (Fig. 3A), and totally four sets of layers constituted of PS and COL were built onto $CaCO_3$ with a particle size of 4-6 µm (Fig. 3B). Initially, the negatively charged $CaCO_3$ particle absorbed positive PS over its surface, shifting its surface charge to positive as a result. This made it easier for negative COL to adsorb over PS from the $CaCO_3$ particle surface. PS and COL were able to be assembled in LBL over $CaCO_3$ particles due to electrostatic adsorption. The zeta potential fluctuation of COL/PS over $CaCO_3$ following each step of assembly is

shown in Fig. 3C. After the construction of PS (positively charged), the zeta potential of the $CaCO_3$ particles changed from -13 mV to 10 mV, and when COL (negatively charged) was assembled over PS from the $CaCO_3$ particle surface in the first batch of assembly, it returned to 12 mV. The subsequent three rounds of assembly, in which $CaCO_3$ was built with PS and COL in order for an additional three times, showed a comparable variation in surface charges, demonstrating the success of both PS and COL assembly.

The chemical bonds and functional groups contained in $(COL/PS)_4@CaCO_3$ and its components were identified using FTIR (Fig. 3D). Vaterite and calcite were responsible for the absorption peaks at 1070 cm^{-1} and 712 cm^{-1}, respectively [41]. Additionally, the calcite peak (712cm^{-1}) rose when comparing $CaCO_3$, $PS@CaCO_3$, and $(COL/PS)@CaCO_3$, indicating that some vaterite underwent calcite transformation. The peak at 1635 cm^{-1} steadily moved to a lower wavenumber as $(COL/PS)_4@CaCO_3$ was assembled, and the peak at 1633 cm^{-1} eventually emerged. It was proven that PS and COL had been successfully coated on the surface of $CaCO_3$ by the absorption band at 1635 cm^{-1}, which was attributable to the stretching vibration of C=O, and 1633 cm^{-1}, which was attributed to the vibration of C=C.

XRD was used to identify the crystallographic changes in the pristine $CaCO_3$ particle and its derivatives (Fig. 3E). Multiple peaks can be found in pristine $CaCO_3$ at 21° (004 crystal plane of vaterite), 24.9° ((1 1 0) crystal plane of vaterite), 27.1° ((1 1

2) crystal plane of vaterite), 32.9° ((1 1 4) crystal face of vaterite), and 43.9° ((3 0 0) crystal face of vaterite) [42]. In addition, there was a diffraction peak at 29.4°, which matched the calcite crystal plane (1 0 4). These peaks demonstrated that compared to calcite, vaterite predominated in pure $CaCO_3$. While some of the vaterite's diffraction peaks vanished during the LBL assembly process, calcite's distinctive new peaks, corresponding to the crystal faces (0 1 2), (1 1 0), (1 1 3), and (2 0 2) of the mineral, appeared at 23.1°, 36.0°, 39.5°, 43.2°, and 47.5°. Conjointly, this demonstrated that some vaterite underwent calcite transformation, which is consistent with FTIR data (Fig. 3D).

The mass of COL/PS constructed over $CaCO_3$ was measured by TGA after the successful assembly of PS and COL on the surface of $CaCO_3$ had been confirmed. In an atmosphere with 20% oxygen and 80% nitrogen, the weight loss of the $(COL/PS)_4@CaCO_3$ sample was shown in Fig. 3F. It was simple to observe the typical three independent weight decreases. The first weight loss, which resulted in a loss of 3.77% at temperatures between 50 and 250 ^oC, should have been caused by the evaporation of mixed and adsorbed water. The second weight loss happened between 250 and 600 ^oC, which is a high temperature that normally initiates the thermal deterioration of common carbon polymers. The 12.83% weight reduction revealed the $(COL/PS)_4@CaCO_3$ sample's COL/PS composition. The last weight loss was caused by the decomposition of $CaCO_3$ to produce CO_2 and happened above 600 ^oC with a rapid fall rate.

The static hydrophilicity and surface morphology of $CaCO_3$ changed during the assembly of PS and COL over $CaCO_3$ to create $(COL/PS)_4@CaCO_3$. The $CaCO_3$'s water contact angle considerably decreased from 116 to 30 ^{o} (Fig. 3G), demonstrating that PS and COL significantly enhanced the $CaCO_3$'s hydrophilic property. Furthermore, the $(COL/PS)_4@CaCO_3$ surface became rougher and uniformly adorned with PS and COL (Fig. 3H), which may aid hemostasis in the application.

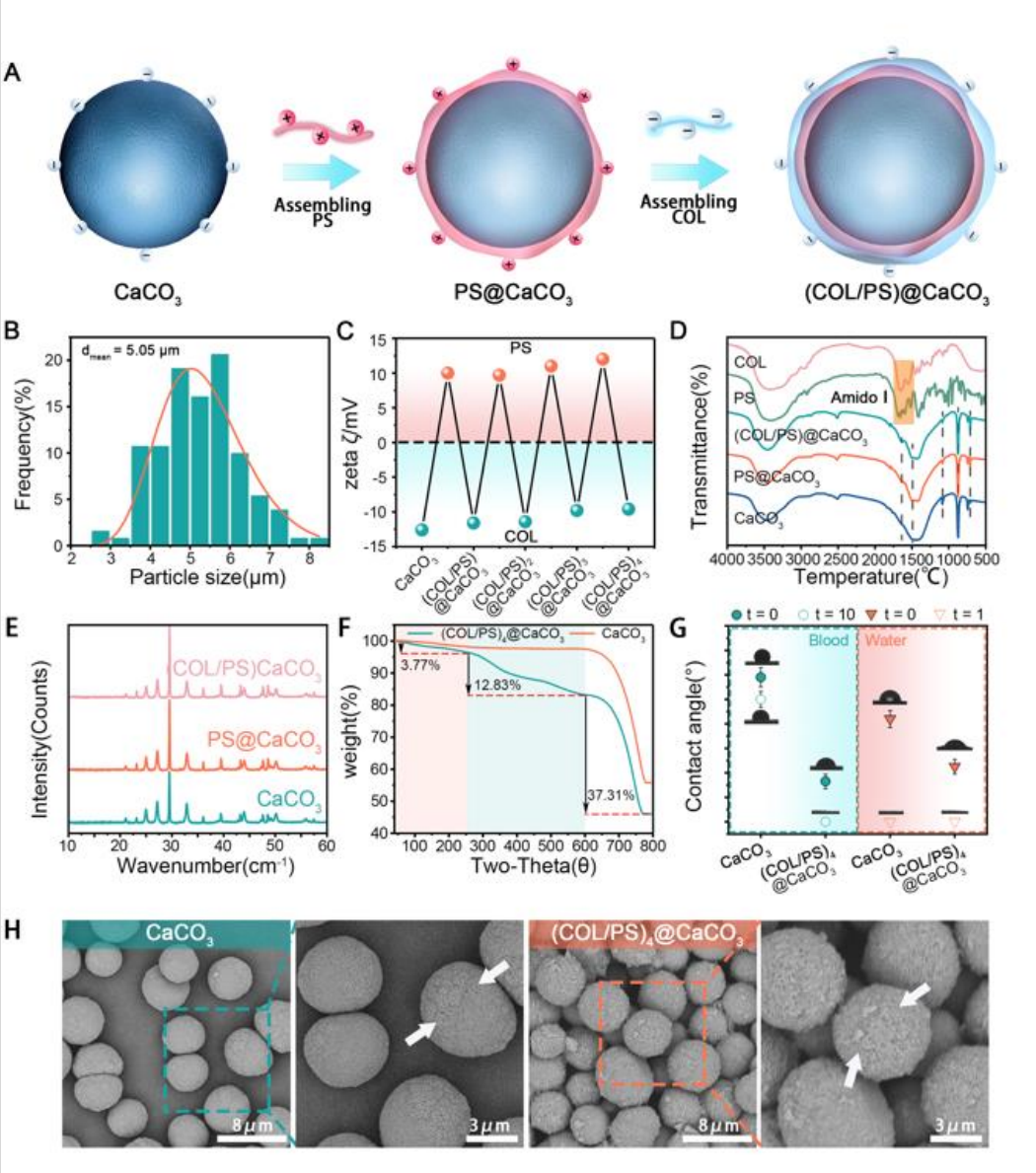

Fig. 3 Characterization. (A) Schematic for the synthesis of $(COL/PS)@CaCO_3$. (B) The

particle size of $CaCO_3$, (C) Zeta-potential as a function of the number of COL/PS layers. (D) FTIR analysis. (E) XRD analysis. (F) TGA. (G) The contact angle of typical materials. (H) SEM images of the $CaCO_3$ and $(COL/PS)_4$@$CaCO_3$.

3.2 Gas-jet propelling performance

Hemostats made of general powder are ineffective for halting bleeding from deep or incompressible lesions. One popular explanation was that blood streaming from the wound's top was likely to flush particle hemostats away, impeding their delivery to the wound's bleeding roots. Therefore, the development of hemostatic particles propelled by a gas jet and capable of deep dives against blood flow was groundbreaking.

The motion behaviors of both $(COL/PS)_4$@$CaCO_3$-T and $(COL/PS)_4$@$CaCO_3$-T-TXA^+ in PBS were examined in order to predict the gas-jet propelling capacity in the wound chamber. For $(COL/PS)_4$@$CaCO_3$-T, there was no apparent horizontal diffusion detected (Fig. 4A); however, for $(COL/PS)_4$@$CaCO_3$-T-TXA^+, there was apparent diffusion driven by quickly formed macro bubbles (Fig. 4B). Similar phenomenon was also observed in an L-shape tube (Video S1). Additionally, $(COL/PS)_4$@$CaCO_3$-T-TXA^+ was initially dyed with the fluorescent green dye FITC in order to further distinguish the motion potentials in the mimic vessels. Further research on its self-propulsion ability was conducted in PBS-filled glass tubes that were positioned at various angles (Fig. 4C).

According to Fig. 4D, the cooperation of (1) the departing force of CO_2 bubbles from the $CaCO_3$ substrates, (2) the upward floating force of free CO_2 bubbles, and (3) the downward gravity of $(COL/PS)_4$@$CaCO_3$-T-TXA^+, caused the distance of gas-jet propelling $(COL/PS)_4$@$CaCO_3$-T-TXA^+ to depend on the angles of the tube placed. Free CO_2 bubbles' upward floating force and $(COL/PS)_4$@$CaCO_3$-T-TXA^+'s downward gravity were more effective in influencing the motion distance of $(COL/PS)_4$@$CaCO_3$-T-TXA^+ when the tube angle was 90° and -90°. Gravity and floating forces, on the other hand, hardly ever affected the horizontal motion of $(COL/PS)_4$@$CaCO_3$-T-TXA^+ when the tube angle was 0°. $(COL/PS)_4$@$CaCO_3$-T-TXA^+ was directly driven to travel horizontally by the CO_2 bubbles that were leaving the $CaCO_3$ substrates. Similar to this, the previously described forces may also be used to explain how different forces affected the travelling distance of particles given from different angles (45° and -45°). These findings implied that $(COL/PS)_4$@$CaCO_3$-T-TXA^+ can be applied to irregularly shaped and incompressible wounds, and damaged blood vessels.

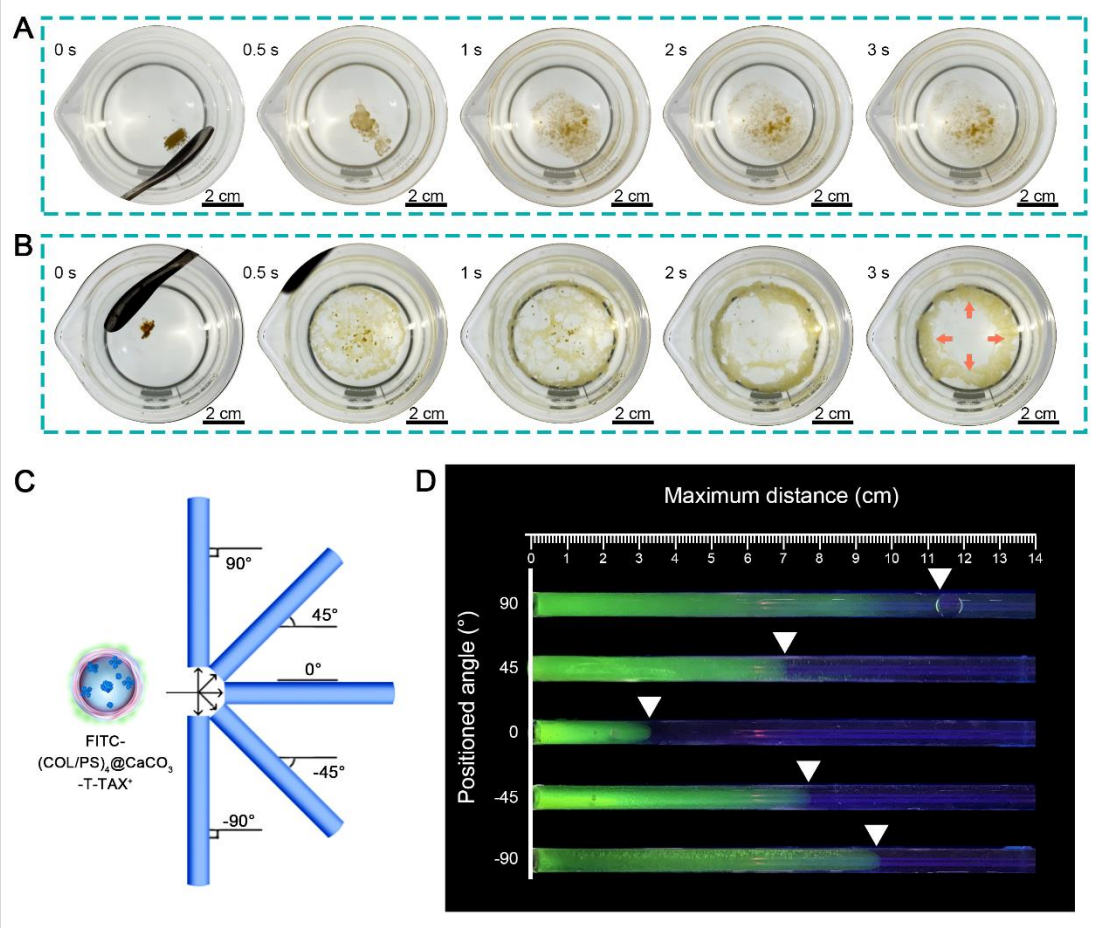

Fig. 4 Images captured after the sprinkling of (A) $(COL/PS)_4@CaCO_3$-T and (B) $(COL/PS)_4@CaCO_3$-T-TXA^+ into PBS. (C) Schematic showing application of FITC-$(COL/PS)_4@CaCO_3$-T-TXA^+ particles onto static liquid at different angles. (D)The maximum gas-jet propelling distance in PBS.

3.3 Blood clotting behavior and *in vitro* hemostasis

The characterization mentioned above has confirmed the successful preparation of $(COL/PS)_4@CaCO_3$ by the assembly of COL/PS over $CaCO_3$. Accordingly, $(COL/PS)_4@CaCO_3$ was used as the hemostatic drug carrier and thrombin, a commonly used commercial hemostatic drug, was used as the loading drug to prepare the final $(COL/PS)_4@CaCO_3$-T sample in order to update its overall hemostatic performance. A

high drug loading capacity of thrombin over $(COL/PS)_4@CaCO_3$-T was shown; the usage efficiency was as high as 54.1% (10.82 U/g).

To determine the fundamental hemostatic characteristics of $(COL/PS)_4@CaCO_3$-T, primary blood clotting was first studied. In a 96-well plate, the total blood's clotting behavior was assessed (Fig. 5A). The order of the clotting speed was $(COL/PS)_4@CaCO_3$-T > $(COL/PS)_4@CaCO_3$ > $CaCO_3$ > TXA > blank, as illustrated in Fig. 5B. The accurate clotting time was also measured using the conventional method [36] . It has been shown that the whole blood's clotting time without additives was around 8.2 min, which is consistent with the findings of an earlier investigation [40]. Both TXA and $CaCO_3$ had poor blood clotting performance, their clotting times were as long as about 7.7 min and 7.2 min respectively. However, clotting time was significantly reduced to 6 ± 0.5 min ($p < 0.001$) after the addition of $(COL/PS)_4@CaCO_3$, and more remarkably, it was reduced to 2 ± 0.6 min ($p < 0.001$) when $(COL/PS)_4@CaCO_3$-T was used (Fig. 5C). These results demonstrated that the assembly of COL/PS enabled enhanced hemostatic property of pristine $CaCO_3$, and the subsequent loading of thrombin over $(COL/PS)_4@CaCO_3$ (the drug carrier) further boosted the blood-clotting ability. This can be explained by the potentials of COL to adsorb blood cells, promote blood cell and platelet aggregation, release platelet-stimulated coagulation factors, and activate endogenous hemostasis [26]; In addition, PS has the ability to dissociate the original antithrombin-heparin complex, restoring regular antithrombin activity [21]. $CaCO_3$ preserved greater hemostatic efficacy after being coated with PS and COL.

A bleeding wound model was created prior to the *in vivo* experiment in order to investigate the hemostatic capacity in full depth. A blood control device was self-constructed to simulate the uncompressible bleeding wound (Fig. 2). When blood was pumped into the bleeding wound model from the inlet, it would directly overflow from the injury point because the outlet was higher than the injury point. However, when the injury point was blocked, blood would pass through the outlet (Fig. 5D), proving that the hemostasis at the injury point was successful. Therefore, bleeding at the outlet can be used to determine the hemostatic capacity. Blood was seen to flow away from the injury point in Fig. 5D, proving that $CaCO_3$ could not cause blood to coagulate. In contrast, when $(COL/PS)_4$@$CaCO_3$-T or $(COL/PS)_4$@$CaCO_3$-T-TXA^+ was applied, blood passed through the outlet 3 min later, proving that blood had successfully coagulated at the injury point. Applied materials over the injury location had a very distinct condition, which was particularly important to note. Particularly, $CaCO_3$ was difficult to blend with the moving blood, which was streaming from the wound and flushing $CaCO_3$ powder away. While only minimal $(COL/PS)_4$@$CaCO_3$-T and little $(COL/PS)_4$@$CaCO_3$-T-TXA^+ were flushed away by gushing blood, $(COL/PS)_4$@$CaCO_3$-T and $(COL/PS)_4$@$CaCO_3$-T-TXA^+ were easier to mix with blood. This may be because $(COL/PS)_4$@$CaCO_3$-T and $(COL/PS)_4$@$CaCO_3$-T-TXA^+ were more blood-compatible owing to the hydrophilic COL/PS layer. More importantly, combining $(COL/PS)_4$@$CaCO_3$-T with blood was a little more difficult than $(COL/PS)_4$@$CaCO_3$-T-TXA^+, which could be instantly mixed with blood to produce

CO_2 macro bubbles. According to histological investigation, $(COL/PS)_4@CaCO_3$-T only remained at the top of the wound (Fig. 5E(a)), while $(COL/PS)_4@CaCO_3$-T-TXA^+ diffused completely throughout the entire wound chamber (Fig. 5E(b)). This demonstrated that the gas-jet propelling function of $(COL/PS)_4@CaCO_3$-T-TXA^+ may be the most important factor in faster hemostasis.

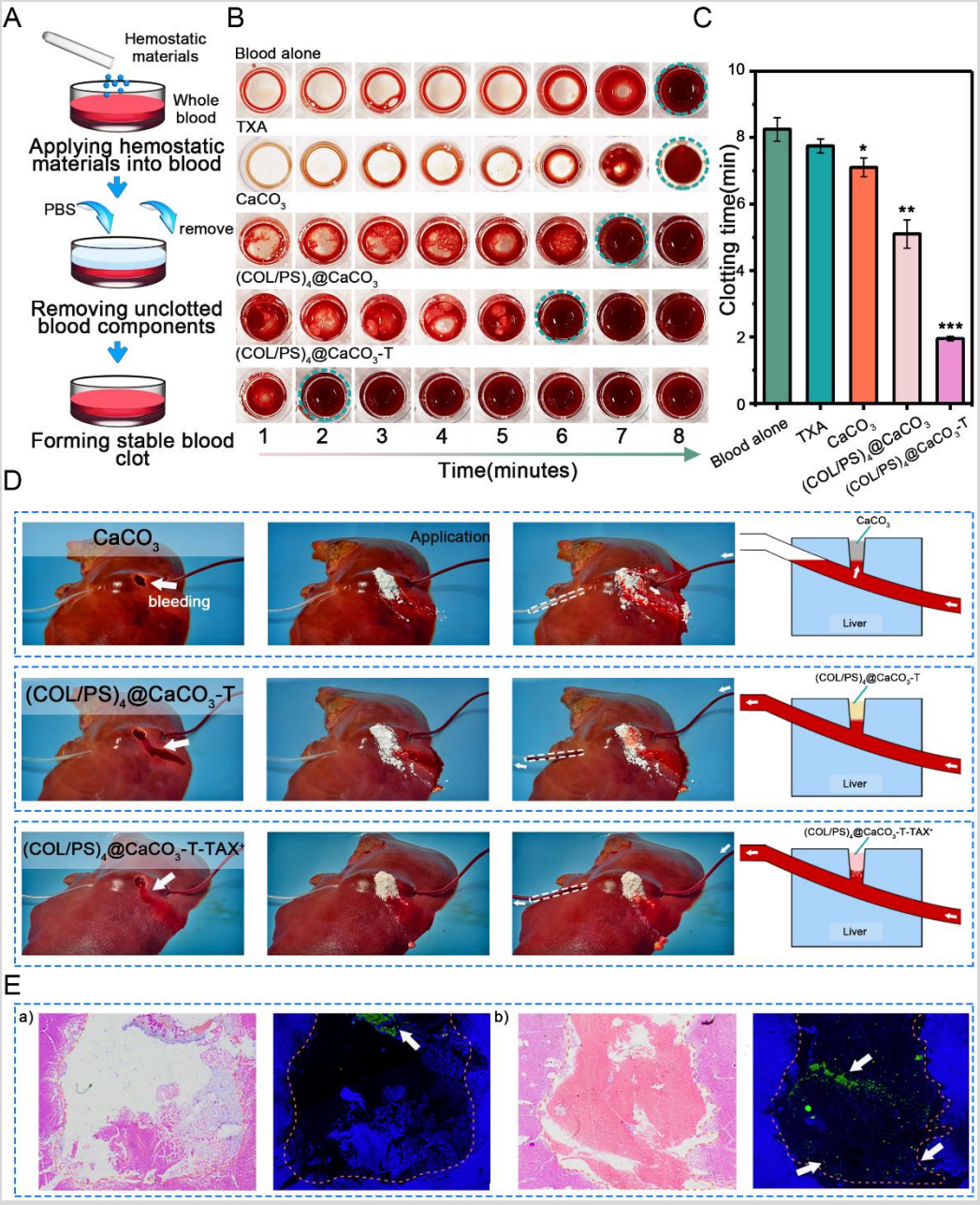

Fig. 5 Blood clotting performance. (A) Schematic of blood clotting in the well plate

method. (B) Photographs of the blood clotting process. (C) clotting time recorded in the well plate method (n = 3). (D) Photographs and diagram of hemostasis mode. (E) HE and MA staining of hemostasis in wounds of the porcine liver. Both $(COL/PS)_4@CaCO_3$-T (a) and $(COL/PS)_4@CaCO_3$-T-TXA^+ (b) were stained with fluorescent green.

3.4 Blood coagulation mechanisms

Understanding the mechanisms underlying blood coagulation was crucial given $(COL/PS)_4@CaCO_3$ has shown to have hemostatic potential. For the mechanism investigation, only samples devoid of thrombin were employed in order to concentrate on the impact of the drug carrier $(COL/PS)_4@CaCO_3$). As a result, whole blood was used to interact with samples of $CaCO_3$, $(COL/PS)_4@CaCO_3$, and $(COL/PS)_4@CaCO_3$-TXA^+ before these samples were examined using SEM. All samples attached to the red blood cells, which displayed biconcave shape, as seen in Fig. 6A. On $(COL/PS)_4@CaCO_3$ and $(COL/PS)_4@CaCO_3$-TXA^+, where cells effectively attached and formed aggregates, the greater number of adhering red blood cells were found; in contrast, pure $CaCO_3$ rarely had any adhered red blood cells. The red blood cells' affinity for $CaCO_3$ was boosted by the assembly of PS and COL over $CaCO_3$, which helped to coagulate blood for hemostasis. A glue-like fibrous net that trapped red blood cells was also seen for $(COL/PS)_4@CaCO_3$-TXA^+ when compared to $(COL/PS)_4@CaCO_3$, which can be explained by the fact that $CaCO_3$ and TXA+ from $(COL/PS)_4@CaCO_3$-TXA^+ were depleted to produce CO_2 and left only glue-like

COL/PS layers.

In the process of coagulation, platelet aggregation and activation are equally as important as the aggregation of blood red cells. Therefore, flow cytometry was used to investigate the activation of platelets. Ca^{2+} and $CaCO_3$ activated only a small percentage of platelets (approximately 5%), as shown in Fig. 6B(c); in contrast, $(COL/PS)_4@CaCO_3$ activated significantly more platelets (six times as many as Ca^{2+} and $CaCO_3$). The construction of COL/PS layers upon naked $CaCO_3$ can be the reason why $(COL/PS)_4@CaCO_3$ can so effectively aggregate platelets.

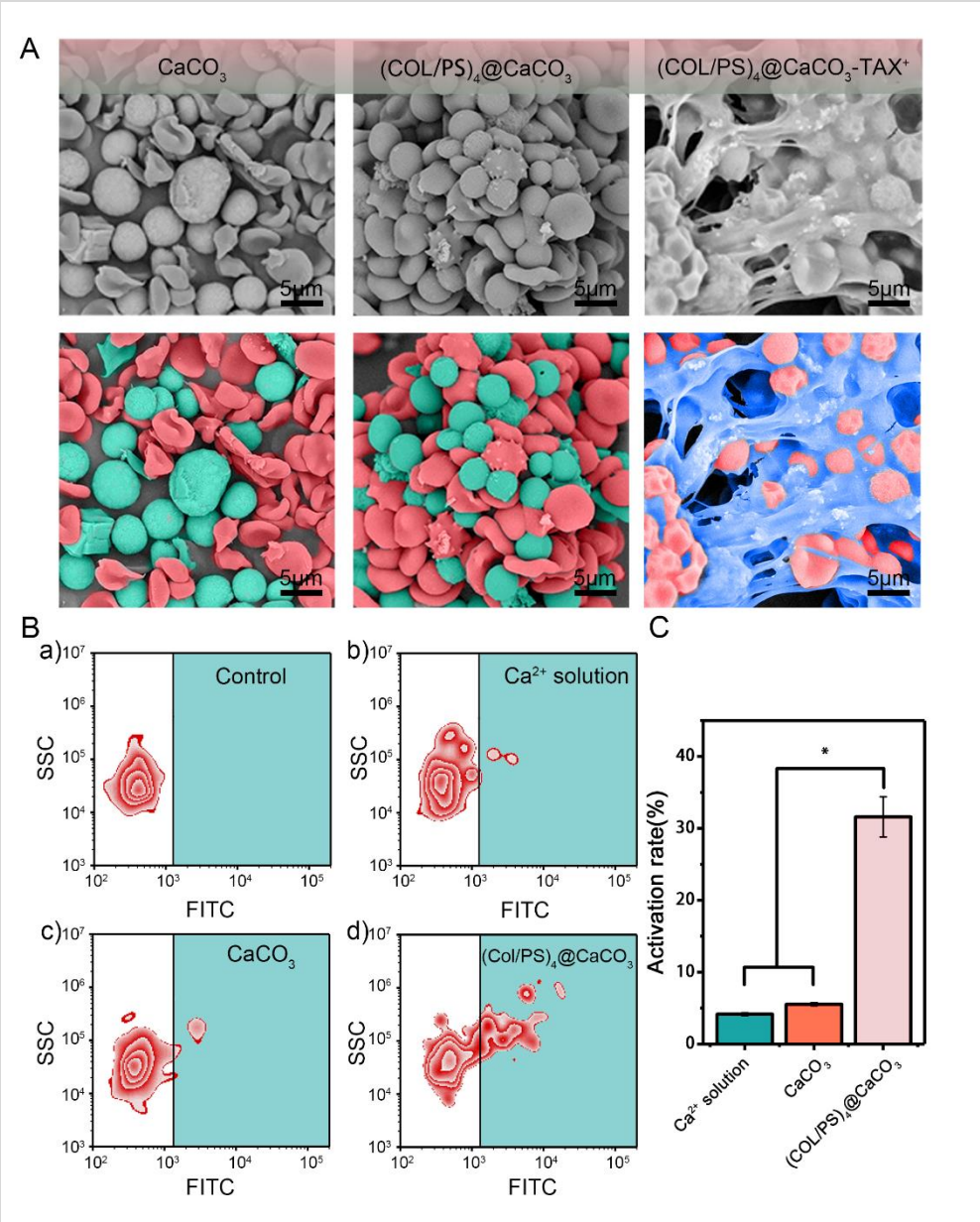

471

472 Fig. 6 Assessment of Blood Coagulation Mechanisms. (A) SEM images of red blood

473 cells (red color) on the surface of different hemostatic materials (cyan-blue color) and

474 COL/PS network (blue color). (B) Flow cytometric assessment: representative zebra

475 plots of activation and aggregation of platelet treating with a) nothing (control), b) Ca^{2+}

476 solution, c) $CaCO_3$, and d) $(COL/PS)_4@CaCO_3$. The activated platelet particles are

477 highlighted in cyan blue. (C) Activation percentage of platelets.

478

3.5 *In vivo* hemostasis

The effectiveness of several hemostatic substances was initially evaluated in vivo using mice tail vein hemorrhage models (Fig. 7A). The bleeding in the tail continued for 4 min in the absence of hemostats. When the bleeding tail vein was treated with $(COL/PS)_4$@$CaCO_3$-T-TXA^+, the hemostatic time was shortened to as little as 30 s (Fig. 7B), which was even 20 s shorter than that of the commercial product Celox™. The hemostatic time of $CaCO_3$ was 3 min, suggesting that $CaCO_3$ has weak hemostatic capacity when used alone. Similar studies were carried out in arteries in addition to hemostasis in veins. After completely cutting the artery, hemostats were immediately applied (Fig. 7C). In comparison to Celox™, $(COL/PS)_4$@$CaCO_3$-T-TXA^+ had a hemostatic time of 30 s, which was only half as long. This suggested that $(COL/PS)_4$@$CaCO_3$-T-TXA^+ was more effective at controlling hemorrhage in arteries as well. Additionally, in vivo hemostasis was performed over a rabbit liver injury model to assess the hemostatic effectiveness of $(COL/PS)_4$@$CaCO_3$-T-TXA^+ in uncompressible bleeding wounds (Fig. 7E). Similar outcomes were discovered. The hemostatic time for the $(COL/PS)_4$@$CaCO_3$-T-TXA^+ sample was 30 s, comparable to Celox™ (Fig. 7F). All of these findings revealed that $(COL/PS)_4$@$CaCO_3$-T-TXA^+ exhibited superior hemostatic properties to Celox™ in the bleeding model of either mouse vein, mouse artery, or rabbit liver. The comprehensive and exceptional hemostatic property gave $(COL/PS)_4$@$CaCO_3$-T-TXA^+ a major potential to challenge Celox™ in practical applications in the future.

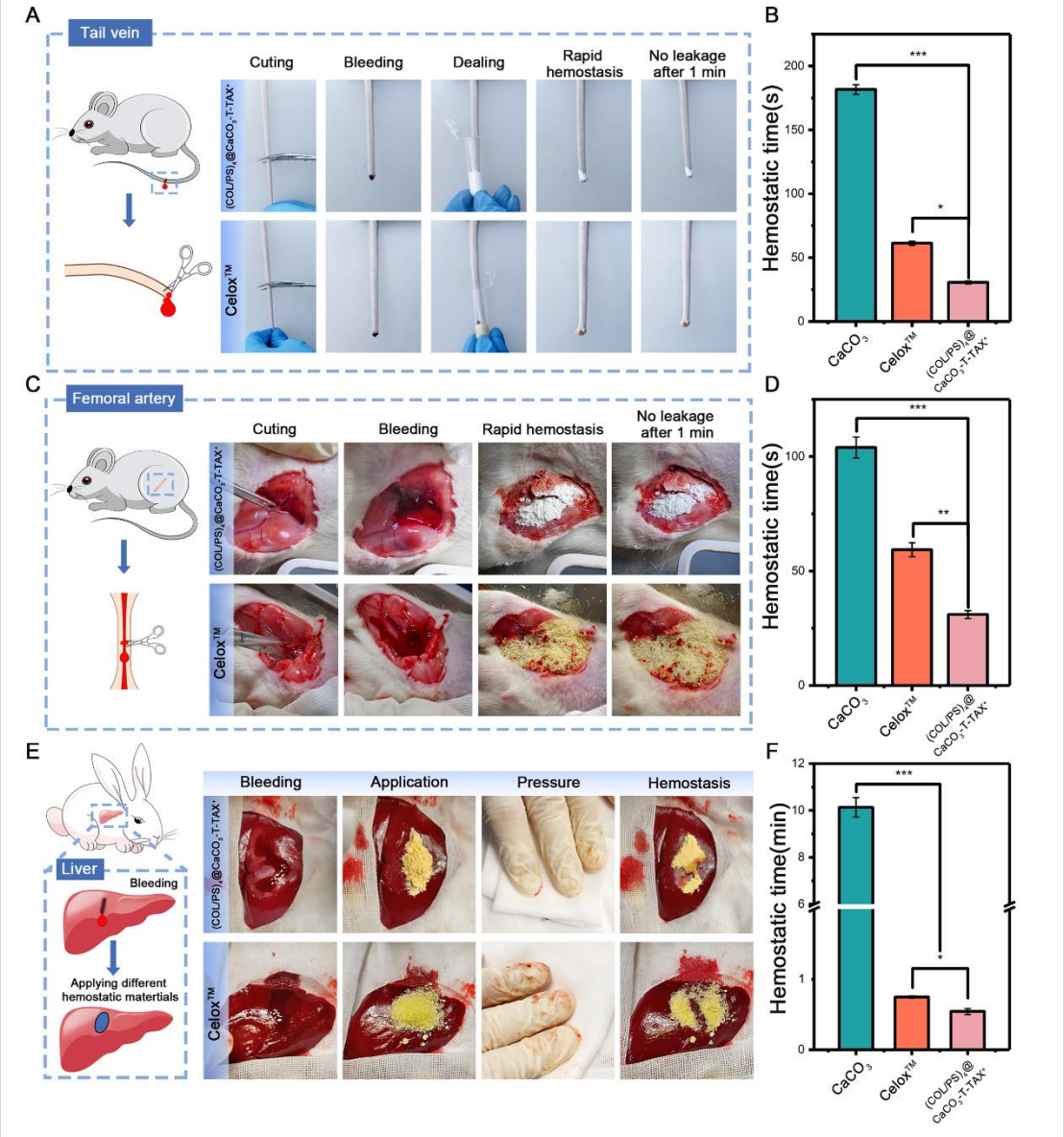

Fig. 7 In vivo hemostatic model. (A) mouse tail vein bleeding model. (B) Hemostatic time in mouse tail vein bleeding models. (C) Mouse femoral artery models. (D) Hemostatic time in mouse femoral artery models. (E) rabbit liver bleeding models. (F) Hemostatic time in rabbit liver bleeding models.

3.6 Biosafety

All hemostats place a high focus on good hemocompatibility. The in vitro hemolysis assay was used to assess the hemocompatibility of $(COL/PS)_4@CaCO_3$. The

supernatants of all samples obtained by centrifugation generally displayed a similar degree of transparency to that of the PBS control group after being co-incubated with various concentrations of $(COL/PS)_4@CaCO_3$ at 37 °C for one hour, and the hemolysis ratios were all less than 4% (Fig. 8A), which is the safe level for hemostatic materials [43].

L929 cells were used to test the cytotoxicity of $(COL/PS)_4@CaCO_3$. As can be shown in Fig. 8B, after being incubated with various doses of $(COL/PS)_4@CaCO_3$ extracts, all of the cells displayed great vitality (>99%). The outstanding biocompatibility of $(COL/PS)_4@CaCO_3$ was demonstrated by the high cell viability of all $(COL/PS)_4@CaCO_3$ samples, even the sample that was co-incubated with L929 cells for 72 h at an 80 g/mL concentration. Additionally, L929 cell proliferation was used to assess cytocompatibility. After one, two, and three days of co-incubation, all groups showed rapid cell proliferation as a result of an increase in the number of living cells (Fig. 8C). All samples showed spindle-shaped morphology in the living cells, which were dyed a green color. The outcome indicated that $(COL/PS)_4@CaCO_3$ displayed strong cytocompatibility because there were comparatively few dead cells stained in red.

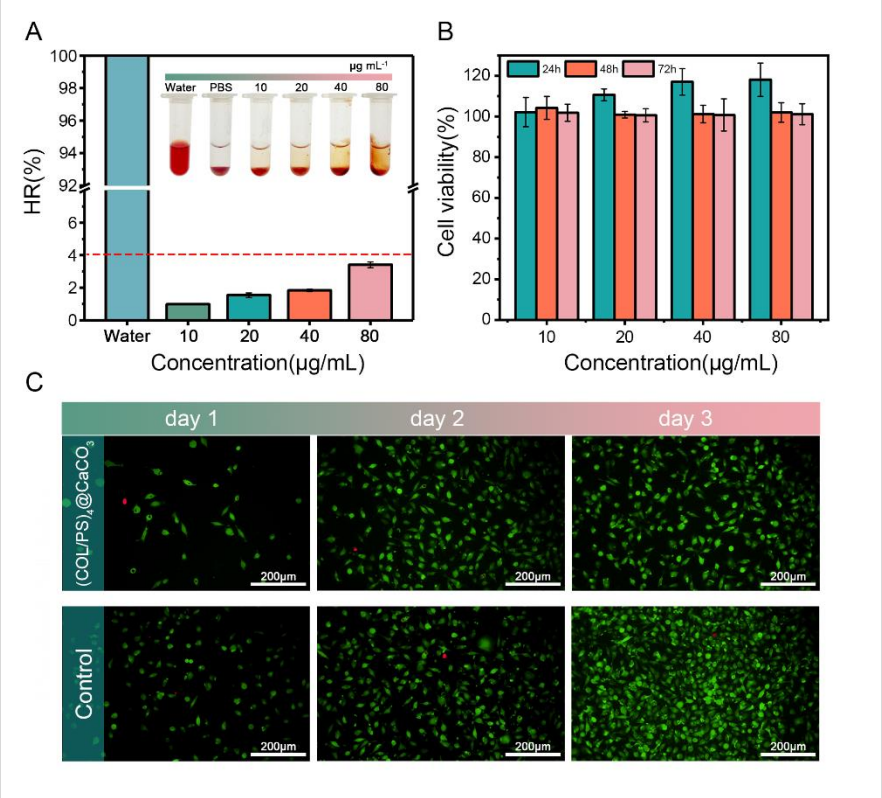

Fig. 8 Cytocompatibility assessment. (A) Hemocompatibility of different concentrations of $(COL/PS)_4@CaCO_3$. (B) Cell viability of L929 cells after incubation with $(COL/PS)_4@CaCO_3$ for 1,2 and 3 days. (C) Live/Dead staining of L929 cells after incubation with $(COL/PS)_4@CaCO_3$ for 1,2 and 3 days. Positive control: cells cultured in medium without materials (n = 3).

Biocompatibility and biodegradability are important considerations since $(COL/PS)_4@CaCO_3$-T-TXA^+ can be employed for in vivo hemostasis [44]. Using Celox™ as a reference, tests on the (COL/biocompatibility PS)4@$CaCO_3$'s and biodegradation were carried out in a rabbit subcutaneous implantation model. In contrast to Celox™, following two weeks of implantation using $(COL/PS)_4@CaCO_3$, the wound swelling was significantly reduced (Fig. 9A). It is clear that

541 $(COL/PS)_4@CaCO_3$ has good biocompatibility because the wound was almost
542 completely healed by Week 8 and eventually reverted to healthy tissue by Week 10.
543
544 Massive amounts of sample residues were found in the tissue in the first two weeks, as
545 evidenced by the histological section (Fig. 9B). The samples' surroundings were
546 covered with a large number of inflammatory cells, which suggested that these
547 reactions started soon after implantation. Since Week 6, there has been an increase in
548 the degradation of $(COL/PS)_4@CaCO_3$; in addition, the number of inflammatory cells
549 has dramatically decreased, and more fibroblasts have emerged, indicating the gradual
550 biodegradation of $(COL/PS)_4@CaCO_3$ in vivo. The $(COL/PS)_4@CaCO_3$ was
551 significantly calcified and absorbed by Week 10; however, there were still remnants of
552 Celox^{TM}, and the tissue inside the wound was loose and had formed a cavity, making
553 tissue repair difficult. These findings demonstrated the outstanding biodegradability of
554 $(COL/PS)_4@CaCO_3$, which can be fully accomplished within ten weeks.
555

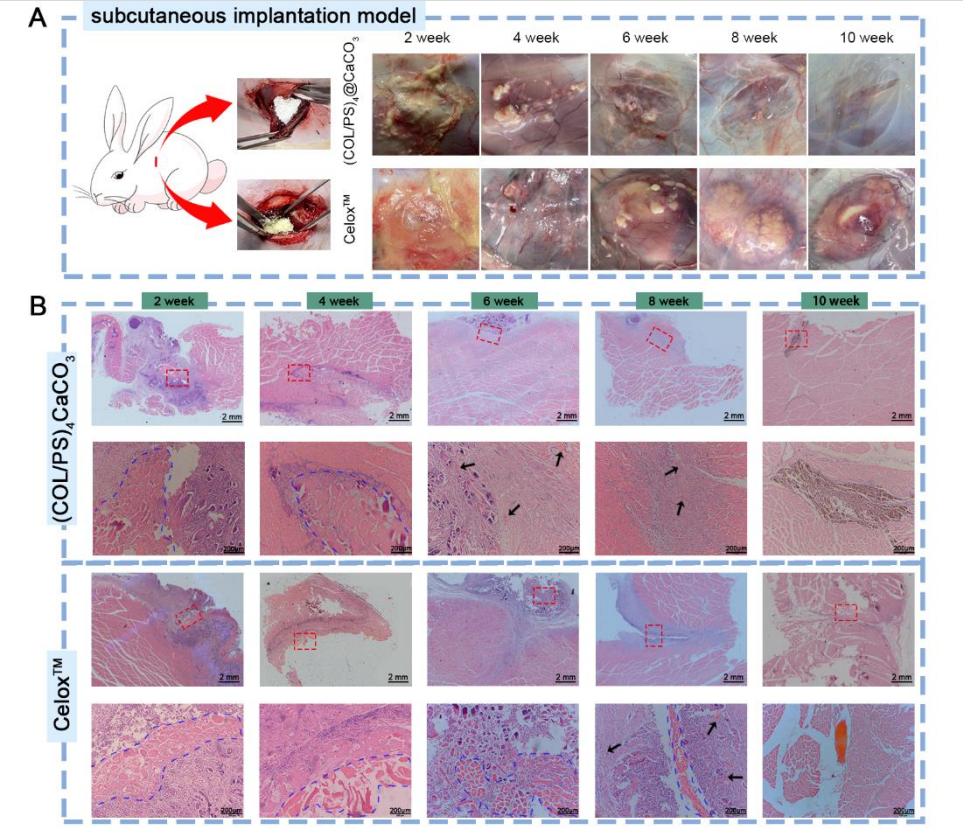

Fig. 9 Biocompatibility and biodegradability evaluation. (A) Implantation of $(COL/PS)_4@CaCO_3$ into muscle tissue. (B) Histological sections from the corresponding muscle tissue. Residues were outlined with blue dash lines; Granulation tissue was outlined with black arrows.

4 Conclusion

Hemostasis remains a significant barrier for complex wounds with irregular shape and incompressibility. The hemostatic effectiveness of conventional hemostats may be noticeably decreased by the flushing impact of gushing blood. In this study, we developed a gas-jet propelled hemostat $(COL/PS)_4@CaCO_3$-T-TXA^+ that was capable of accurately delivering hemostatic medications to deep bleeding sites against blood flow in complex wounds while still resisting the flushing impact of gushing

blood. Both the mouse and rabbit hemorrhage models demonstrated excellent hemostatic properties, with the bleeding in both animals ceasing within 30 s. Additionally, in the subcutaneous muscle plant model, the hemostats can be entirely degraded in eight weeks. In light of this, $(COL/PS)_4$@$CaCO_3$-T-TXA^+ was a promising hemostat with intelligent and targeted delivery of hemostatic drugs in complicated bleeding wounds with irregular shape and incompressibility. It would present a fresh method for powdered hemostats to effectively stop bleeding in wounds with gushing blood.

Acknowledgements

This work was supported by the Natural Science Foundation of Chongqing, China (cstb2022nscq-msx0555, cstc2020jcyj-msxmx0024, and cstc2020jcyj-msxmx0383), and the National Natural Science Foundation of China (No. 52103096).

Reference

1. J. Ju, S. Jin, S. Kim, J. H. Choi, H. A. Lee, D. Son, H. Lee and M. Shin, *ACS Applied Materials & Interfaces*, 2022, **14**, 25115-25125.
2. Y. Huang, X. Zhao, C. Wang, J. Chen, Y. Liang, Z. Li, Y. Han and B. Guo, *Chemical Engineering Journal*, 2022, **427**, 131977.
3. P. Zhao, Y. Feng, Y. Zhou, C. Tan and M. Liu, *Bioactive Materials*, 2023, **20**, 355-367.
4. C. Hana, K. Deeb, K. DeSuza, S. G. Smith, S. Ivanov and L. Lit, *Blood*, 2020, **136**, 27-28.

5. V. K. Frantz, H. T. Clarke and R. Lattes, 1944, **120**, 170-198.
6. Y. Zhang, J. Guan, J. Wu, S. Ding, J. Yang, J. Zhang, A. Dong and L. Deng, *Carbohydrate Polymers*, 2019, **219**, 405-413.
7. Z. Li, A. Milionis, Y. Zheng, M. Yee, L. Codispoti, F. Tan, D. Poulikakos and C. H. Yap, *Nature Communications*, 2019, **10**, 5562.
8. Z. G. Wu, W. Zhou, W. J. Deng, C. L. Xu, Y. Cai and X. Y. Wang, *ACS APPLIED MATERIALS & INTERFACES*, 2020, **12**, 20307-20320.
9. Y. Hong, F. Zhou, Y. Hua, X. Zhang, C. Ni, D. Pan, Y. Zhang, D. Jiang, L. Yang, Q. Lin, Y. Zou, D. Yu, D. E. Arnot, X. Zou, L. Zhu, S. Zhang and H. Ouyang, *Nature Communications*, 2019, **10**, 2060.
10. X. Peng, X. Xu, Y. Deng, X. Xie, L. Xu, X. Xu, W. Yuan, B. Yang, X. Yang, X. Xia, L. Duan and L. Bian, *Advanced Functional Materials*, 2021, **31**.
11. Q. Li, E. Hu, K. Yu, M. Lu, R. Xie, F. Lu, B. Lu, R. Bao and G. Lan, *Bioact Mater*, 2021, **6**, 4625-4639.
12. J. Jun, R. C. Millican, J. A. Sherwood, B. S. Tucker, V. M. Vijayan, G. C. Alexander, V. Thomas, B. C. Brott and P. T. J. Hwang, *ACS Applied Bio Materials*, 2020, **3**, 3137-3144.
13. Y. Liang, C. Xu, F. Liu, S. Du, G. Li and X. Wang, *ACS Applied Materials & Interfaces*, 2019, **11**, 23848-23857.
14. C. Xu, Y. Yan, J. Tan, D. Yang, X. Jia, L. Wang, Y. Xu, S. Cao and S. Sun, 2019, **29**, 1808146.
15. Y.-Q. Niu, J.-H. Liu, C. Aymonier, S. Fermani, D. Kralj, G. Falini and C.-H. Zhou, *Chemical Society Reviews*, 2022, **51**, 7883-7943.
16. J. Xing, Y. Cai, Y. Wang, H. Zheng and Y. Liu, *Advances in Polymer Technology*, 2020, **2020**, 8749238.
17. P. F. Ferrari, E. Zattera, L. Pastorino, P. Perego and D. Palombo, *International Journal of Biological Macromolecules*, 2021, **177**, 548-558.
18. P. Wang, R. K. Kankala, J. Fan, R. Long, Y. Liu and S. Wang, *Journal of Materials Science: Materials in Medicine*, 2018, **29**, 68.
19. M. Xie, F. Zhang, L. Liu, Y. Zhang, Y. Li, H. Li and J. Xie, *Applied Surface Science*,

2018, **440**, 853-860.
20. X. Feng, J. Wang, P. Cai, Z. Yang, J. Shen, Y. Zhang and X. Zhang, *Colloids and Surfaces A: Physicochemical and Engineering Aspects*, 2021, **625**, 126977.
21. I. Ruseska, K. Fresacher, C. Petschacher and A. Zimmer, 2021, **11**, 1508.
22. S. Cao, G. Xu, Q. Li, S. Zhang, Y. Yang and J. Chen, *Composites Part B: Engineering*, 2022, **234**, 109746.
23. X.-k. Ouyang, L. Zhao, F. Jiang, J. Ling, L.-Y. Yang and N. Wang, *Carbohydrate Polymers*, 2022, **293**, 119688.
24. M. Dai, M. Li, J. Gong, L. Meng, B. Zhang, Y. Zhang, Y. Yin and J. Wang, *Materials & Design*, 2022, **216**, 110577.
25. X. Xie, D. Li, Y. Chen, Y. Shen, F. Yu, W. Wang, Z. Yuan, Y. Morsi, J. Wu and X. Mo, 2021, **10**, 2100918.
26. Y. He, J. Wang, Y. Si, X. Wang, H. Deng, Z. Sheng, Y. Li, J. Liu and J. Zhao, *International Journal of Biological Macromolecules*, 2021, **178**, 296-305.
27. S. Zhang, J. Li, S. Chen, X. Zhang, J. Ma and J. He, *Carbohydrate Polymers*, 2020, **230**, 115585.
28. F. Cheng, C. Liu, H. Li, X. Wei, T. Yan, Y. Wang, Y. Song, J. He and Y. Huang, *Carbohydrate Polymers*, 2018, **183**, 246-253.
29. C. Ding, M. Tian, R. Feng, Y. Dang and M. Zhang, *ACS Biomaterials Science & Engineering*, 2020, **6**, 3855-3867.
30. P. U. Muñoz-González, M. C. Lona-Ramos, L. D. Gutiérrez-Verdín, G. H. Luévano-Colmenero, F. Tenorio-Rocha, R. García-Contreras, G. González-García, A. Rosillo-de la Torre, J. Delgado, L. E. Castellano and B. Mendoza-Novelo, *Biomedical Materials*, 2022, **17**, 045005.
31. A. J. Lausch, L. C. Chong, H. Uludag and E. D. Sone, 2018, **28**, 1804730.
32. J.-t. Gu, K. Jiao, J. Li, J.-f. Yan, K.-y. Wang, F. Wang, Y. Liu, F. R. Tay, J.-h. Chen and L.-n. Niu, *Bioactive Materials*, 2022, **15**, 68-81.
33. G. M. Seon, M. H. Lee, B.-J. Kwon, M. S. Kim, M.-A. Koo, D. Kim, Y. Seomun, J.-T. Kim and J.-C. Park, *Acta Biomaterialia*, 2017, **48**, 175-185.
34. Y. Sang, M. Roest, B. de Laat, P. G. de Groot and D. Huskens, *Blood Reviews*,

2021, **46**, 100733.

35. S. M. Park, D. R. Kang, J. H. Lee, Y. H. Jeong, D. A. Shin, S. Yi, Y. Ha and K. N. Kim, *World Neurosurgery*, 2021, **154**, e215-e221.

36. W.-F. Lu, T.-Y. Lu, Y.-C. Liu, T.-H. Liu, C.-C. Feng, C.-W. Lin, K.-C. Yang, Y. Wei and J. Yu, *ACS Applied Nano Materials*, 2021, **4**, 12798-12806.

37. Y. Liu, K. Yu, S. Shang, R. Xie, F. Lu, R. Bao, G. Lan and E. Hu, *Nanoscale*, 2021, **13**, 9843-9852.

38. L. Yao, H. Gao, Z. Lin, Q. Dai, S. Zhu, S. Li, C. Liu, Q. Feng, Q. Li, G. Wang, X. Chen and X. Cao, *Chemical Engineering Journal*, 2022, **428**, 131005.

39. R. Zhou, Y. Zhou, J. Cheng, J. Cao, M. Li, H. Yu, D. Wei, B. Li, Y. Wang and Y. Zhou, *Materials Today Bio*, 2022, **16**, 100380.

40. Z. Shi, G. Lan, E. Hu, F. Lu, P. Qian, J. Liu, F. Dai and R. Xie, *Chemical Engineering Journal*, 2022, **427**.

41. J. A. Juhasz-Bortuzzo, B. Myszka, R. Silva and A. R. Boccaccini, *Crystal Growth & Design*, 2017, **17**, 2351-2356.

42. Q. Hu, J. Zhang, H. Teng and U. Becker, *American Mineralogist*, 2012, **97**, 1437-1445.

43. L. Zheng, Q. Wang, Y. S. Zhang, H. Zhang, Y. Tang, Y. Zhang, W. Zhang and X. Zhang, *Chemical Engineering Journal*, 2021, **416**, 129136.

44. A. Mahmoodzadeh, J. Moghaddas, S. Jarolmasjed, A. Ebrahimi Kalan, M. Edalati and R. Salehi, *Chemical Engineering Journal*, 2021, **418**, 129252.